

# Cryogenic X-ray detectors for synchrotron science

Stephan Friedrich

Advanced Detector Group, Lawrence Livermore National Laboratory, 7000 East Avenue, L-270, Livermore, CA 94550, USA, and Advanced Biological and Environmental X-ray Facility, Lawrence Berkeley National Laboratory, 1 Cyclotron Road, MS 6-2100, Berkeley, CA 94720, USA.  
 E-mail: friedrich1@llnl.gov

Cryogenic detectors operated at temperatures below 1 K offer an order of magnitude higher energy resolution than conventional semiconductor-based energy-dispersive detectors, and orders of magnitude higher efficiency than grating spectrometers. Initially developed for astrophysics applications, these detectors are increasingly used in synchrotron-based research, both for detector characterization and for high-resolution X-ray spectroscopy. This article reviews current cryogenic detector technologies and their performance with respect to their use in synchrotron science. It also discusses areas of research that can benefit from improved energy resolution detectors, and outlines desirable detector developments in the context of novel science they would enable.

**Keywords:** superconducting X-ray detectors; microcalorimeters; superconducting tunnel junctions; fluorescence-detected X-ray absorption spectroscopy.

## 1. Introduction: why cryogenic detectors at the synchrotron?

In synchrotron-based X-ray spectroscopy there are two energy scales that determine the choice of spectrometer in a given application. One is set by the natural line-width of the X-ray emission lines and their shifts in different chemical states of the element. They vary between one-tenth to several eV, and chemical state analysis by X-ray spectroscopy thus requires spectrometers with accordingly high energy resolution. In X-ray emission spectroscopy this resolution is provided by grating or crystal spectrometers, while in X-ray absorption spectroscopy (XAS) it is provided by the monochromatic incident beam. The other energy scale is set by the energy difference between characteristic X-ray emission lines from different elements in the sample, typically tens to hundreds of eV. Elemental analysis thus only requires X-ray spectrometers with a resolution sufficient to separate them and detect them above the spectral background, and semiconductor Ge or Si(Li) detectors are typically being used in this application.

An additional requirement on the spectrometer relates to the concentration  $c_x$  of the element  $x$  of interest. High concentration samples, a term loosely used here to describe samples with  $c_x \geq 1\%$ , can be analyzed both with grating and semiconductor spectrometers. Lower concentration samples usually require semiconductor detectors because their large solid angle coverage is needed to capture a significant fraction of the weak fluorescence (Fig. 1). For this reason, semiconductor detectors are also widely used in fluorescence-detected XAS, a technique that combines the high energy

resolution of the monochromatic beam with the moderate energy resolution of the semiconductor detector for elemental specificity to measure chemical states of dilute samples.

Cryogenic detectors are a class of energy-dispersive X-ray spectrometers operated at temperatures around 0.1 K (Gatti, 2004; Frank *et al.*, 2003; d'Acapito & Maurizio, 2004). They offer an order of magnitude higher energy resolution than semiconductor Ge or Si(Li) detectors, although not as high as grating spectrometers. On the other hand, cryogenic detectors also offer orders of magnitude higher detection efficiency than grating spectrometers, although not as high as semiconductor detectors. In addition, cryogenic detectors do not have a surface dead layer, and can therefore provide very high peak-to-background ratios, even at low energies (Fig. 2). They are

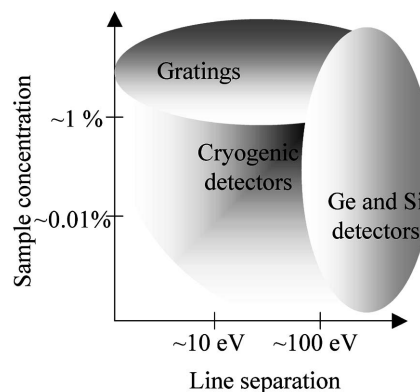


**Figure 1**  
 Schematic classification for research with different spectrometer types in terms of line separation and sample concentration.

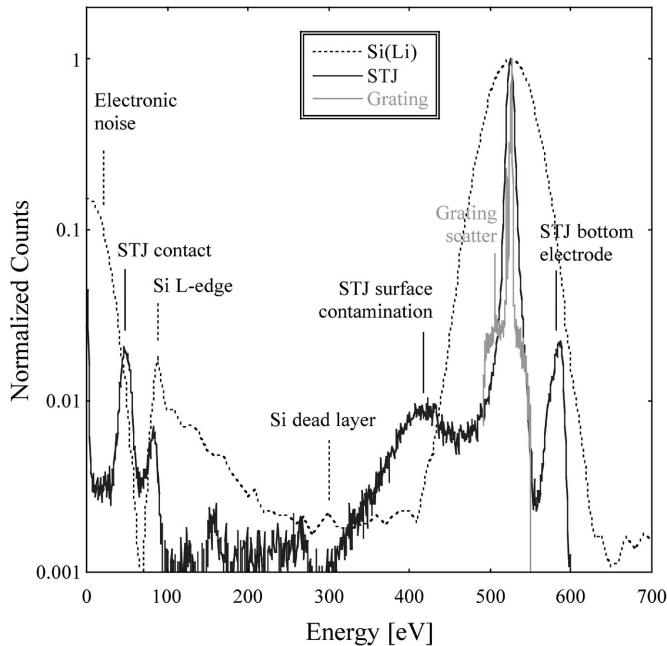


**Figure 2** Comparison of the response function of semiconductor, cryogenic and grating spectrometers at an energy  $E_x = 0.5$  keV. (The performance of different spectrometers at 6 keV is shown in Fig. 7.)

therefore advantageous in applications that require either a good rejection of the spectral background, or higher energy resolution than semiconductor detectors and higher efficiency than gratings. Here we discuss some of the science that cryogenic spectrometers can enable, review the physics and the performance of different cryogenic detector technologies, and outline future spectroscopy applications that make additional detector developments desirable.

## 2. Science with cryogenic detectors

### 2.1. Light-element X-ray fluorescence analysis

Elemental analysis is the most basic application in X-ray spectroscopy, based on the fact that each element emits X-rays with different energies. Except for hydrogen, characteristic X-rays from all elements can be detected indicating the presence of an element, and their intensity can be used to quantify its concentration. Different measurement configurations can provide additional information, such as elemental maps in scanning beam experiments, three-dimensional elemental distributions in X-ray tomography, or surface composition in total X-ray reflection fluorescence analysis. X-ray fluorescence (XRF) analysis is widely used in all areas of science. XRF of light elements, defined here as the elements from lithium to fluorine ( $3 \leq Z \leq 9$ ), requires detectors with high energy resolution and high peak-to-background (P/B) ratio, since fluorescence lines are separated by only  $\sim 100$  eV, and any spectral background reduces the signal-to-noise (S/N) ratio. High resolution and high P/B ratio are especially important for the analysis of dilute elements, since the low-energy fluorescence of light elements is weak, and the small

signal  $S$  must be separated from background fluctuations. Cryogenic X-ray spectrometers can increase the sensitivity for light-element XRF analysis, since they combine high energy resolution and low spectral background with high quantum efficiency.

To quantify spectrometer sensitivity, we consider the general case when a sample of thickness  $d$  contains an element of interest  $x$  with absorption coefficient  $\mu_x$  that fluoresces at energy  $E_x$  with a yield  $\varepsilon_x$ . If this sample is illuminated with a beam of intensity  $I_0$  at energy  $E_0$  for an acquisition time  $\tau$ , the signal counts  $S_x$  recorded by a detector with solid angle coverage  $\Omega_{\text{det}}/4\pi$  and quantum efficiency  $\eta_{\text{det}}$  is given by (Jaklevic *et al.*, 1977)

$$S_x = I_0 \tau \frac{\mu_x(E_0) \varepsilon_x}{\mu_{\text{tot}}(E_0) + \mu_{\text{tot}}(E_x)} \times (1 - \exp\{-[\mu_{\text{tot}}(E_0) + \mu_{\text{tot}}(E_x)]d\}) \Omega_{\text{det}} \eta_{\text{det}} / 4\pi. \quad (1)$$

The expression  $\mu_x(E_0)/[\mu_{\text{tot}}(E_0) + \mu_{\text{tot}}(E_x)]$  is the fraction of the incident beam absorbed by the element  $x$  for a total absorption  $\mu_{\text{tot}}$ , and scales with sample concentration. The term  $\mu_{\text{tot}}(E_x)$  in the denominator accounts for re-absorption of the fluorescence signal in the sample. For light elements with fluorescence energies below 1 keV, absorption lengths  $1/\mu_{\text{tot}}$  are of the order of micrometers, and typical samples are therefore in the thick limit  $d \gg 1/[\mu_{\text{tot}}(E_0) + \mu_{\text{tot}}(E_x)]$  where the exponential in equation (1) is negligible. If the sample is dilute, *i.e.*  $\mu_x \ll \mu_{\text{tot}}$ , the total absorption is dominated by the background and the signal  $S_x$  is linearly proportional to the absorption  $\mu_x(E_0)$  by the element  $x$ .

To compare spectrometer technologies and their sensitivity, we consider the case when the signal  $S_x$  is affected by a spectral background  $B$  and additional fluorescence from element  $y$  at energy  $E_y$  with  $S_y$  counts. We assume that the spectrometer response is Gaussian, and characterized by its full width at half-maximum,  $\Delta E_{\text{FWHM}}$ . The spectral background  $B$  is due to non-idealities of the spectrometer response and is assumed to be constant. In this case the limiting statistical r.m.s. noise  $N_x$  and  $N_y$  can be determined analytically (Ryder, 1977) according to

$$N_x^2 = aB + bS_x + cS_y, \quad N_y^2 = aB + bS_y + cS_x, \quad (2)$$

with

$$\begin{aligned} a &= \Delta E_{\text{FWHM}} \pi^{1/2} / [(2 \ln 2)^{1/2} (1 - d^2)], \\ b &= (2 - 4d^{7/3} + 2d^{10/3}) / [3^{1/2} (1 - d^2)^2], \\ c &= (2d^{4/3} - 4d^{7/3} + 2d^2) / [3^{1/2} (1 - d^2)^2], \\ d &= \exp[-2 \ln 2 (E_x - E_y)^2 / \Delta E_{\text{FWHM}}^2]. \end{aligned}$$

Equation (2) describes the statistical noise contribution in the limiting case that systematic errors are negligible. It quantifies this limit in terms of line separation  $E_x - E_y$  and detector resolution  $\Delta E_{\text{FWHM}}$ , which enter through the parameters  $d$  and  $a$ . The parameter  $a$  describes the influence of the background  $B$  on the noise, and correctly reduces to  $N_{x,y} \propto \Delta E_{\text{FWHM}}^{1/2}$  when background statistics dominate the spectrum, *i.e.* in the limit  $d \rightarrow 0$  and  $B \gg (S_x + S_y)$ . The parameter  $c$

quantifies the influence of the overlap of one line on the precision for measuring the other line. As expected,  $c \rightarrow 0$  for well separated lines since  $d \rightarrow 0$  for  $E_x - E_y \gg \Delta E_{FWHM}$ .

Fig. 3 shows the signal-to-noise ratio  $S_x/N_x$  according to (2) as a function of energy resolution for sample concentrations of 10%, 1% and 0.1%. The total number of counts is  $10^7$ , corresponding to an acquisition time  $\tau = 15$  s at a rate of  $\sim 600.000$  counts  $s^{-1}$ . For each sample concentration the S/N ratio is plotted for the case of negligible spectral background ( $B = 0$ ), and for constant P/B ratios of 100 and 10. Even in dilute samples the spectrometer resolution  $\Delta E_{FWHM}$  matters mostly when it is worse than about half the line separation  $E_y - E_x$ , in which case the S/N ratio degrades roughly proportional to  $\Delta E_{FWHM}$  or  $\Delta E_{FWHM}^2$  depending on the relative magnitude of the lines and the degree of line overlap (Ryder, 1977; Drury & Friedrich, 2005). If the energy resolution is sufficient to fully separate the two lines, the signal-to-noise ratio is independent of  $\Delta E_{FWHM}$  and approaches  $1/(N_x)^{1/2}$  according to Poisson's statistics, provided the background  $B$  is negligible. Otherwise, the S/N ratio degrades proportional to  $(\Delta E_{FWHM})^{1/2}$ , since the influence of the background is increased when the signal counts are spread out over a wider energy window. Note that fluorescence yields are rather low for soft X-ray energies below 1 keV, varying between  $\varepsilon_x \simeq 0.1\%$  and  $\sim 1\%$  and thus easing the requirements on the total count rates of the spectrometer.

The sensitivity of different spectrometer technologies for light-element XRF analysis depends on their energy resolution, maximum count rate, detection efficiency and P/B ratio. Table 1 summarizes the performance at 0.5 keV for 'typical' and for 'state-of-the-art' instruments. The 'typical' Ge detector describes the average performance of a large commercial 30-element Ge spectrometer (Canberra, www.canberra.com). The current 'best' Ge detector, an attri-

**Table 1**

Comparison of spectrometer performance at 0.5 keV.

All values are approximate.

Detector	Resolution $\Delta E_{FWHM}$ (eV)	Count rate (counts $s^{-1}$ )	Efficiency $\eta\Omega/4\pi$	P/B ratio
Ge (typical)	130	$3 \times 10^5$	0.1	50:1
Ge (best)	60	$3 \times 10^4$	0.03	200:1
STJ (typical)	20	$10^5$	$10^{-4}$	200:1
STJ (best)	10	$10^6$	$10^{-3}$	1000:1
Grating (typical)	0.5	$10^5$	$10^{-6}$	200:1
Grating (best)	0.2	$10^6$	$10^{-5}$	1000:1
Grating with optic	0.2	$10^6$	$3 \times 10^{-4}$	200:1

bute chosen solely based on achieved resolution at 0.5 keV, is a single-channel Ge detector optimized for low-energy performance (Gresham Scientific Instruments, www.gsinst.com; Lepy *et al.*, 2000). Its P/B ratio is limited by a  $\sim 15$  nm dead layer at the contact electrode. The 'typical' cryogenic detector describes the performance of a nine-pixel superconducting tunnel junction (STJ) spectrometer during routine operation at the synchrotron (Friedrich *et al.*, 2001). The 'best' STJ combines achieved energy resolution (le Grand *et al.*, 1998) and P/B ratios (Bechstein *et al.*, 2004) with the efficiency and count-rate capabilities of a current 36-pixel upgrade. There is no unavoidable dead layer in STJ detectors. While the small detector size limits its solid-angle coverage, it allows placing most of the STJ array at an angle of  $90^\circ$  to the incident beam, thereby limiting elastic scatter and maintaining a high P/B ratio. Grating spectrometers are typically optimized for spectroscopy and routinely achieve sub-eV resolution below 1 keV (Nordgren & Guo, 2000), at the expense of low efficiency. However, the efficiency can be improved by using a point-to-parallel X-ray optic before the diffraction grating with large cone angles (www.parallax-x-ray.com), a technique than can also be applied to cryogenic spectrometers (Wollman *et al.*, 2000). The P/B ratio is typically set by scattered X-rays (*cf.* Fig. 2).

Fig. 4 shows the signal-to-noise ratio for the analysis of the light elements Li through F ( $3 \leq Z \leq 9$ ) at a concentration of 1% for different spectrometer types calculated according to (2). The only spectral interference is assumed to arise from a constant background and from oxygen fluorescence at 525 eV, except for the case of measurements on dilute oxygen itself, where it is assumed to be due to nitrogen. The signal rate is given by (1) using the spectrometer characteristics from Table 1 and literature values of the fluorescence yield (Krause, 1979), constrained by the maximum detector count rate. Note that the S/N ratio for analysis of the very light elements will be decreased due to X-ray absorption in the IR-blocking windows in front of the detector, which is not accounted for in the simulations. In general, the S/N ratio improves slightly for the heavier elements because of the higher fluorescence yield  $\varepsilon_x$  and thus higher signal rates, with somewhat lower S/N ratios for N and F whose emission lines are near the interfering oxygen *K* fluorescence at 525 eV. The 36-pixel detector upgrade significantly enhances the sensitivity of cryogenic STJ spectrometers because of the higher detection efficiency and

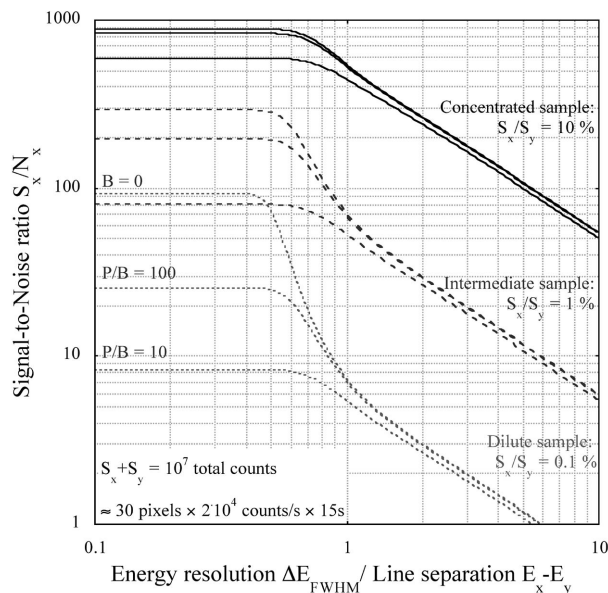


**Figure 3**  
Signal-to-noise ratio as a function of spectrometer resolution for different sample concentrations and P/B ratios according to equation (2).

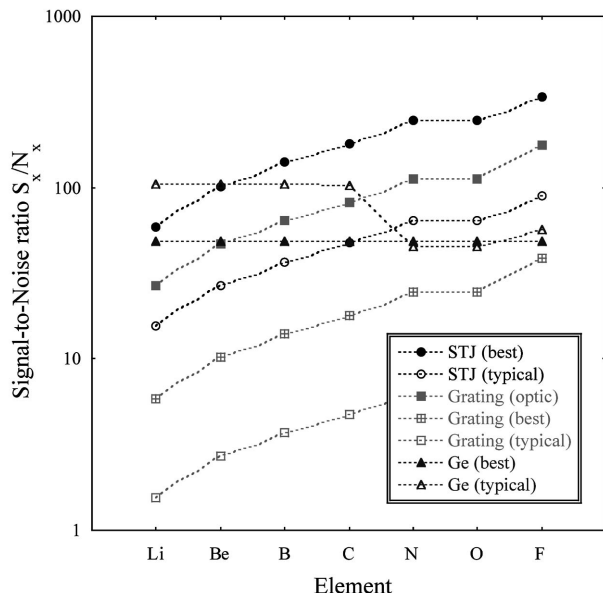


**Figure 4**  
S/N ratio according to equations (1) and (2) for light-element XRF analysis for different spectrometer types, assuming a sample concentration of 1% and a data acquisition time of 15 s. Spectrometer parameters are taken from Table 1.

count-rate capabilities. Future increases in array size will further increase the STJ spectrometer sensitivity.

In general, high-resolution STJ spectrometers are preferred for XRF analysis with soft X-rays where line overlap is more common and fluorescence yields are low, while conventional high-efficiency Ge or Si(Li) spectrometers are preferred for hard X-rays where their energy resolution is sufficient, their P/B ratio is high, and higher fluorescence yield requires higher count-rate capabilities. Cryogenic spectrometers therefore enhance the sensitivity of light-element XRF analysis.

**2.2. Fluorescence-detected XAS: light-element K-edges and transition metal L- and M-edges**

The chemical state and bonding environment of dilute elements can be analyzed by fluorescence-detected XAS. In these experiments the energy levels of the element of interest are sampled with natural-linewidth-limited resolution by scanning the energy  $E_0$  of the monochromatic incident beam through an appropriate absorption edge. The sensitivity is greatly increased if the subsequent fluorescence is recorded as a measure of the absorption, since the number of background counts can be greatly reduced when windowing on the fluorescence signal of interest (Jaklevic *et al.*, 1977). This requires a detector with sufficient energy resolution to separate the weak X-ray signal from the matrix background fluorescence, and with sufficient solid-angle coverage and P/B ratio to detect the signal above the background within an acceptably short data acquisition time. Cryogenic detectors increase the sensitivity for fluorescence-detected XAS whenever Ge detectors lack energy resolution and grating spectrometers lack detection efficiency. This is often the case for soft X-ray analysis on

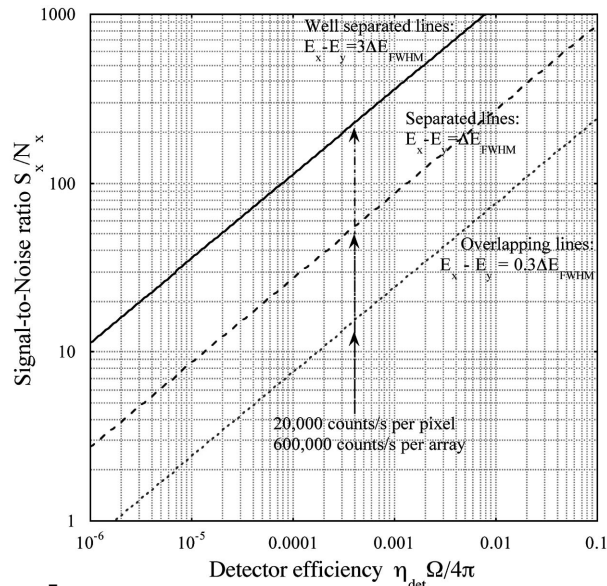


**Figure 5**  
S/N ratio as a function of spectrometer efficiency according to equations (1) and (2) for different degrees of line overlap, assuming a dilute sample concentration  $S_x = 0.01S_y$ , an incident flux  $I_0 = 10^{12}$  photons  $s^{-1}$ , a fluorescence yield  $\epsilon = 10^{-3}$  and an acquisition time  $\tau = 15$  s. This acquisition time per excitation energy corresponds to a  $\sim 1$  h acquisition time for a  $\sim 200$  step X-ray absorption spectrum.

dilute light-element K-edges and on transition metal L- and M-edges (Fig. 1).

One common concern about using cryogenic detectors in such applications is their comparably small size of order  $\sim 0.2$  mm  $\times$  0.2 mm and low count-rate capability, currently limited to  $\sim 20000$  counts  $s^{-1}$  pixel $^{-1}$  for the fastest among them. However, this count rate is sufficient even on undulator beamlines at third-generation synchrotron sources, because fluorescence yields are below  $\sim 1\%$  for soft X-rays, and because detector operation at 0.1 K limits the solid-angle coverage per pixel as it prevents placing the detector arbitrarily close to the room-temperature sample. Fig. 5 quantifies the S/N ratio that can be achieved as a function of detection efficiency, *i.e.* the product of solid-angle coverage  $\Omega/4\pi$  and quantum efficiency  $\eta_{det}$  per pixel, for a dilute sample according to (1) and (2) for different cases of line overlap. The incident flux is  $I_0 = 10^{12}$  photons  $s^{-1}$ , the fluorescence yield is  $\epsilon = 10^{-3}$ , and the spectrometer parameters are taken from Table 1. The overall efficiency of  $10^{-4}$  to  $10^{-3}$  for small cryogenic detector arrays is perfectly fine to acquire absorption spectra from  $\sim 1000$  ppm samples with  $S/N > 100$  within an acceptable period of time without exceeding the maximum count rate, provided that there is no interference from neighboring fluorescence lines.

As an example, we consider sample analysis by X-ray absorption near-edge spectroscopy (XANES) on the first-row transition metals Sc, Ti, V, Cr, Mn, Fe, Co, Ni, Cu and Zn. They are comparably abundant in the earth's crust, and the elements from Ti to Cu can be present in more than one oxidation state. They play important roles as trace elements in the metabolic processes in cells, or as dopants in novel semi-conducting or magnetic materials. Some of them, like Cr, Mn

and Fe, are also of significant environmental concern because of their toxicity and oxidative or absorptive influence on other environmental contaminations. Scientific questions often center on the chemical state of the transition metal and its changes under specific conditions, and *L*-edge XANES is a sensitive element-specific probe of that state (de Groot *et al.*, 1990; Cramer *et al.*, 1991). The *L*-series X-ray emission lines of first-row transition metals range from 395 eV for Sc to 1012 eV for Zn. Unfortunately there are often line overlap problems in that energy range, *e.g.* due to strong oxygen *K* fluorescence at 525 eV. Fig. 6 shows the S/N ratio that can be attained in XANES spectra on transition metals, assuming that the only spectral interference originates from a strong oxygen line at 525 eV (Drury & Friedrich, 2005). Since the absorption coefficient  $\mu_x$  of the element of interest increases at its absorption edges by a factor of  $\sim 10$ , the signal  $S_x = 0.01S_y$  describes samples with a concentration of  $\sim 1000$  ppm. In general, the S/N ratio increases slightly for the heavier elements because of the higher fluorescence yield  $\epsilon_x$  and thus higher signal rates, with lower S/N ratios for V, Cr and Mn whose emission lines are near the interfering oxygen *K* fluorescence at 525 eV. For the elements Sc and Fe to Zn, 30-element Ge spectrometers (triangles) offer higher sensitivity than typical nine-pixel STJ spectrometers, because they efficiently capture the weak signal with high S/N ratio as long as there are no large interfering fluorescence lines nearby. STJ spectrometers (circles) are favorable for the elements Ti to Mn because they can separate their weak metal fluorescence from the interfering O *K* line, with lower efficiency than Ge spectrometers, but sufficient to acquire XAS spectra with high S/N ratio within a  $\sim 1$  h scan. The 36-pixel detector upgrade significantly enhances the sensitivity of STJ spectrometers because of the higher detection efficiency and count-rate

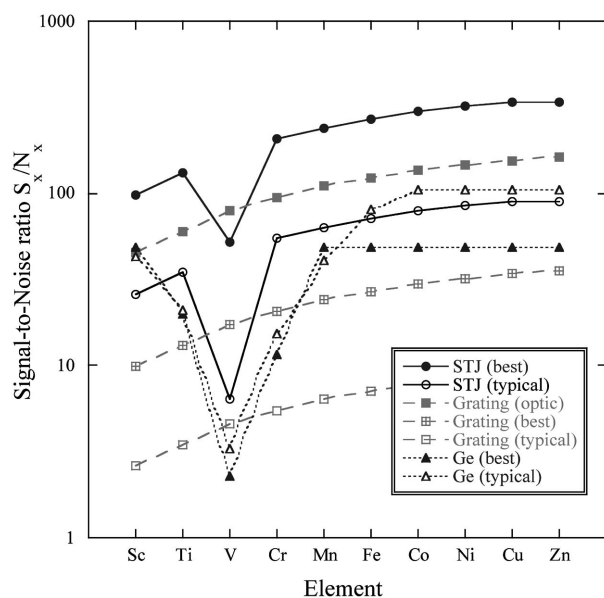


**Figure 6**  
S/N ratio for analyzing *L*-series X-rays of first-row transition metals with a concentration of  $\sim 1000$  ppm for data acquisition time of 15 s per spectrum, *i.e.*  $\sim 1$  h per 200-step scan. Spectrometer parameters are taken from Table 1.

capabilities (solid circles). The development of larger arrays will further enhance the sensitivity of cryogenic spectrometers.

### 2.3. Site-selective and spin-selective EXAFS and XANES

Many samples, especially in the biomedical and environmental sciences, are not homogeneous but contain one element in different chemical species. Often only one of these species, or the difference of site characteristics in a heterogeneous compound, is of scientific interest. Metalloproteins, for instance, can contain Fe in their catalytic center, but also contain Fe–S clusters in other parts of the protein responsible for electron transport. Many environmental samples contain contaminations of the same metal from more than one source, such as Cr from welding, plating operations and natural sources. Novel materials often contain dissimilar sites for binding the same element, such as nitrogen or amphoteric carbon dopants in semiconductors. Chemical separation of different sites is usually difficult, and often impossible without sacrificing the sample integrity.

Site-selective (Grush *et al.*, 1995) or spin-selective (Peng *et al.*, 1994) EXAFS and XANES is an interesting extension of fluorescence-detected XAS that separates the signal from the same element in different bonding environments. It relies on separating the fluorescence signal due to one metal species from the fluorescence of the same metal in a different oxidation or spin state. These measurements can currently only be performed with grating or crystal spectrometers, since chemical shifts of X-ray emission lines are rarely above a few eV, and often much less (Fig. 7). Notable exceptions are cases when different emission lines originate from different oxidation or spin states. For example, in Mn(II) complexes the  $K\beta'$  lines derive from final states with antiparallel net spins between the  $3p^5$  hole and the  $3d^5$  valence shell, while the  $K\beta_{13}$  region is dominated by spin-parallel final states (Peng *et al.*, 1994). In Mn, the  $K\beta'$  and the  $K\beta_{13}$  region are separated by  $\sim 16$  eV. Also, X-ray transition of certain elements can exhibit comparably large chemical shifts, such as the  $K\beta''$  and the  $K\beta_{25}$  lines in Mn, which can shift by up to 5 eV for different oxidation states (Bergmann, Horne *et al.*, 1999; Bergmann *et al.*, 2001). This is within the range to be resolved by current cryogenic microcalorimeters (Fig. 7). However, the lines that exhibit the strongest dependence on chemical state are often weak and accompanied by other significantly stronger emission. For cryogenic detectors to find widespread applications in site- or spin-selective XAS, additional improvements in both energy resolution and total count-rate capabilities are therefore desirable.

### 2.4. Resonant inelastic X-ray spectroscopy (RIXS)

Resonant inelastic X-ray emission is a second-order optical process in which a core electron is excited into the valence band, and the subsequent hole is resonantly filled with a lower-shell electron. The energy difference between incoming and resonantly emitted X-rays is equal to the corresponding soft X-ray absorption energy. RIXS therefore allows the analysis of soft X-ray transitions using hard X-rays. This combines the

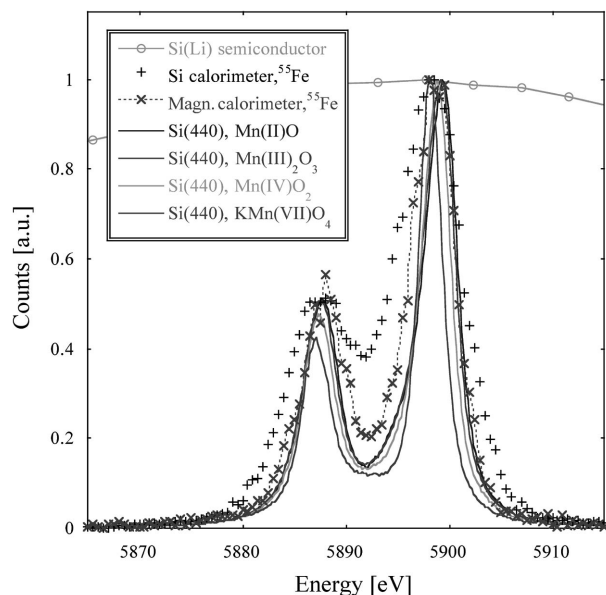


**Figure 7** Comparison of detector performance at 5.9 keV using Mn  $K\alpha_{1,2}$  fluorescence. The spectrum for the cryogenic Si calorimeter with an energy resolution of 5.7 eV FWHM is a summed composite from the 36-channel array launched on the X-ray satellite ASTRO-E2 in 2005 (Stahle *et al.*, 2004; Porter *et al.*, 2005). Magnetic microcalorimeters have achieved an energy resolution of 3.4 eV at 5.9 keV (Fleischmann *et al.*, 2004). The four fluorescence spectra for manganese samples in different oxidation states taken with a Si(440) crystal spectrometer are shown for comparison. Note that  $K\beta$  lines exhibit larger chemical shifts with oxidation state than  $K\alpha$  lines (Bergmann *et al.*, 1999).

high chemical sensitivity of soft X-rays with the ease of atmospheric pressure operation and high fluorescence yield of hard X-rays (Kotani & Shin, 2001). So far, only grating and crystal spectrometers have sufficient energy resolution for RIXS experiments, since chemical information is contained in the fine structure of the energy levels of the subshell and requires an energy resolution of the order of 1 eV. The detection efficiency is low, and the fluorescence analyzer must be scanned over the energy range of the X-ray emission for each excitation energy of the incident beam. This requires high incident flux and long data acquisition times, which can cause radiation damage and currently limits RIXS experiments to concentrated samples.

Cryogenic detectors could greatly improve the detection efficiency for RIXS and shorten the required acquisition time, since the entire emission spectrum can be captured simultaneously. This requires an energy resolution sufficient to resolve fine structure in the hard X-ray subshells, which will be different for each element, but will generally fall in the range 0.5–5 eV. It also requires that the high fluorescence yield for hard X-rays does not produce a photon flux that exceeds the detector’s maximum count rate. Hard X-ray fluorescence yields easily exceed 10% (Krause, 1979), producing count rates above  $10^6$  counts  $s^{-1}$  pixel $^{-1}$  for an incident flux of  $10^{12}$  photons  $s^{-1}$  even if each pixel only covers a solid angle  $\Omega/4\pi \simeq 10^{-5}$ . Such a count rate for an energy resolution of order 1 eV may be difficult to achieve. Still, RIXS with cryogenic detectors would be very interesting, especially for the

analysis of biological and environmental samples that are often dilute and sensitive to radiation damage. Hard X-rays penetrate much more deeply into samples, and therefore deposit their energy over a larger volume and tend to cause less radiation damage than soft X-rays, despite the fact that the energy per photon is higher. While cryogenic detectors will likely be used for some RIXS applications, it remains to be seen if technologies can be developed whose energy resolution and count-rate capabilities are sufficient to make them a widely used tool in this field of synchrotron science.

### 3. Cryogenic detectors

Cryogenic detectors are a class of energy-dispersive detectors with very high energy resolution operated at temperatures of  $\sim 0.1$  K. Low-temperature operation is fundamentally required for high energy resolution because it reduces thermal fluctuations and allows the exploitation of small excitation energies  $\varepsilon$ . Several cryogenic detector technologies have been developed over the last two decades. These developments were initially driven by X-ray astrophysics and dark matter searches, but more recently additional applications in material science and biophysics have emerged. Cryogenic detectors generally fall into two categories: thermal/equilibrium detectors and athermal/non-equilibrium detectors. Thermal detectors, often referred to as microcalorimeters or bolometers, detect the increase in temperature upon X-ray absorption as a measure of X-ray energy. They offer the highest energy resolution, at the expense of lower count-rate capabilities, and are therefore the preferred technology in astrophysics applications. Athermal detectors are similar to conventional semiconductor Ge and Si(Li) detectors in that they record the number of excess non-equilibrium charge carriers excited by X-ray absorption. Athermal detectors have a somewhat lower energy resolution than microcalorimeters, but can be operated at much higher count rates, and have therefore been preferred at the synchrotron. Here we discuss the current performance of the different technologies, possible future developments, and their relevance for synchrotron-based science.

#### 3.1. Thermal detectors: microcalorimeters

Thermal detectors consist of an X-ray absorber with heat capacity  $C$  and a sensitive thermometer, both weakly coupled to a cold bath through a thermal conductance  $G$ . X-ray absorption increases the absorber temperature by  $\Delta T \simeq E_x/C$  in proportion to the X-ray energy  $E_x$ , which is measured by the thermometer, before the absorber and the thermometer cool back down to the bath temperature through the thermal conductance. In the simplest case, *i.e.* when absorber and thermistor are either identical or sufficiently well coupled to act as a single thermal unit, thermal fluctuations  $4k_B T^2 G$  across the thermal conductance limit the energy resolution of microcalorimeters to

$$\Delta E_{\text{FWHM}} \simeq 2.355\xi(k_B T^2 C)^{1/2}. \quad (3)$$

Here  $\xi$  is a dimensionless parameter of order unity that depends on the temperature dependence of the heat capacity, resistance and thermal conductance of the sensor materials (Moseley *et al.*, 1984). Equation (1) can be qualitatively understood considering that thermal detectors are based on the measurement of phonons with an average energy of  $\sim k_B T$ . An absorber at temperature  $T$  contains a total energy  $\sim CT$  and thus a total number of  $\sim CT/k_B T \simeq C/k_B$  phonons. Assuming Poisson's distribution, this number of phonons will fluctuate by  $(C/k_B)^{1/2}$ , causing r.m.s. energy fluctuations of  $(k_B T^2 C)^{1/2}$ . Equation (1) is the thermal analog to the expression  $(F \varepsilon E_x)^{1/2}$  that describes the statistical limit for semiconductor detectors, considering that thermal detectors are based on the measurement of uncorrelated ( $F = 1$ ) phonons ( $\varepsilon = k_B T$ ) and that the fluctuations of the absorber background energy  $CT$  dominate over those of the X-ray energy  $E_x \ll CT$ . For typical operating temperatures  $T \simeq 0.1$  K and absorber volumes around  $\sim 0.001$  mm<sup>3</sup>, microcalorimeters can have an energy resolution of a few eV FWHM at 6 keV (Moseley *et al.*, 1984).

Microcalorimeters are intrinsically slow, since the thermal coupling  $G$  between the sensor and the cold bath is weak at low temperatures, typically of the order of  $\sim 1$  nW K<sup>-1</sup>. Thermal pulse decay times  $\tau \simeq C/G$  are proportional to the absorber volume and thus to the energy range for which the detector is optimized. Typical microcalorimeter decay times are of the order of  $\sim 1$  ms depending on the detector design, although calorimeters optimized for optical photons can have very small heat capacities  $C$  and therefore be made much faster.

### 3.1.1. Semiconductor detectors: doped Si and NTD Ge.

The oldest and most mature cryogenic high-resolution X-ray detectors are based on doped semiconductor thermistors. Both doped Si and neutron transmutation doped (NTD) Ge have been successfully developed for X-ray astrophysics over the last two decades, and detectors with an energy resolution below 5 eV FWHM at 6 keV are now available for space and laboratory astrophysics (Bandler *et al.*, 2000; Silver *et al.*, 2000; Stahle *et al.*, 2004). They rely on a very high sensitivity  $\partial R/\partial T$ , and are fundamentally limited by the phonon noise  $4k_B T^2 G$  across the weak thermal link according to (3). A separate high- $Z$  absorber with heat capacity  $C_{\text{abs}}$  is typically attached to the sensor to increase the absorption efficiency while minimizing the associated increase in noise. This increased noise is due to the finite thermal conductance  $G_{\text{abs}}$  between the absorber and the sensor, and reduces the limiting energy resolution to

$$\Delta E_{\text{FWHM}} \simeq 2.355 (4k_B T^2 C_{\text{abs}})^{1/2} \left[ \frac{G}{G_{\text{abs}}} + \left( \frac{G}{G_{\text{abs}}} \right)^2 \right]^{1/4}, \quad (4)$$

where  $G_{\text{abs}}$  is of the order of  $\sim 10$  nW K<sup>-1</sup> (Bühler *et al.*, 1994; Hoevers *et al.*, 2000). Si and NTD Ge detectors can be optimized for different energy ranges by choosing absorber material and volume. In fact, Si-based thermistors with  $500 \mu\text{m} \times 500 \mu\text{m} \times 25 \mu\text{m}$  Sn absorbers and an energy resolution of 90 eV at 32 keV were the first cryogenic detectors ever oper-

ated at a synchrotron to measure Compton profiles in Si (Stahle *et al.*, 1992). Early on, NTD Ge had the practical advantage over Si of very homogeneous doping, but with recent deep-implant technology Si has mostly caught up. 36-channel arrays of Si thermistors with  $400 \mu\text{m} \times 400 \mu\text{m} \times 7 \mu\text{m}$  HgTe absorbers and an average energy resolution of 5.4 eV at 6 keV have been launched on the Suzaku X-ray astronomy mission in July 2005 (Fig. 7), where they have unfortunately not been able to record any data due to a failure of the cryogenic system in space (Stahle *et al.*, 2004; Porter *et al.*, 2005).

Cryogenic semiconductor detectors are high-impedance devices, and can be read out with low-noise field-effect transistor (FET) preamplifiers, typically operated at  $\sim 100$  K to reduce thermal noise and as close to the  $\sim 0.1$  K detector as possible to minimize capacitance. High-resolution operation restricts the absorber heat capacity to  $\sim 10$  pJ K<sup>-1</sup> according to (4) and thus to absorber volumes around  $\sim 0.001$  mm<sup>3</sup>. This leads to pulse decay times of  $\tau \simeq C_{\text{abs}}/G_{\text{abs}} \simeq 1$  ms, which is acceptable for many astrophysics applications, but probably too slow for most synchrotron science.

### 3.1.2. Superconducting-to-normal transition edge sensors.

In 1995, cryogenic detector research changed with the reinvention of electrothermal feedback for transition edge sensor (TES) microcalorimeters based on superconductors operated at the phase transition between the superconducting and normal state (Andrews *et al.*, 1942; Irwin, 1995). TESs have the unique advantage that their resistance increases with temperature at the superconducting-to-normal transition, as compared with semiconductor detectors whose resistance decreases with increasing  $T$ . This allows the exploitation of electrothermal feedback (ETF) when voltage-biasing the TES, *i.e.* the effect that an increase in TES temperature is counteracted by a decrease in bias power  $P = V^2/R_{\text{TES}}$ . This reduces the intrinsic thermal fluctuations and improves the achievable energy resolution to

$$\Delta E_{\text{FWHM}} \simeq 2.355 [4k_B T^2 C (n/2)^{1/2} / \alpha]^{1/2}, \quad (5)$$

where  $\alpha \cong T/R_{\text{TES}} \partial R_{\text{TES}}/\partial T$  is a dimensionless measure of the TES sensitivity and  $n$  is the exponent in the temperature dependence of the thermal conductance  $G \cong \partial P^{n+1}/\partial T$  (Irwin, 1995). In addition, ETF decreases the pulse decay time by a factor  $\sim \alpha/n$ , and allows operating TESs with different transition temperatures at the same bath temperature  $T_0 \ll T_{\text{TES}}$ , since the TES will be self-biased in the transition at the resistance where the bias power  $V^2/R_{\text{TES}}$  balances the heat flow into the cold bath  $(T_{\text{TES}} - T_0)G$ . Under typical TES operating conditions,  $\alpha \simeq 100$  and  $n \simeq 4$  to 5, and TES microcalorimeters theoretically offer a factor of  $\sim 10$  improvement in energy resolution and speed over Si and NTD Ge-based detectors. Currently, the best TES microcalorimeter detectors have achieved an energy resolution below 2.4 eV FWHM at 6 keV, and pulse decay times of the order of  $\sim 100 \mu\text{s}$  (Ullom *et al.*, 2005). This sets maximum count rates to a few 100 counts s<sup>-1</sup> per detector pixel (Wollman *et al.*, 2000).

TESs must have very low resistances, typically well below  $1 \Omega$ , to ensure fast and homogeneous thermalization of the X-ray energy to reduce spatial variations in the detector response and electrothermal stability (Irwin *et al.*, 1998). This necessitates the use of superconducting quantum interference device (SQUID) preamplifiers, which do not have any voltage noise. While SQUIDS are more expensive and less widely available than FETs, they are becoming a mature technology with several commercial suppliers now offering SQUID readout for  $\sim \$1000$  per channel. In addition, several low-temperature multiplexing technologies are being developed to read out more than one detector pixel with a single SQUID preamplifier, thereby increasing detector area and count-rate capabilities without increasing the heat load into the spectrometer cold stage (Irwin, 2002; Cunningham *et al.*, 2002). Among the *thermal* cryogenic detectors, superconducting TESs are currently the most likely technology to find applications at the synchrotron despite their only moderate count rate because they combine high energy resolution with multiplexed readout for array operation.

**3.1.3. Magnetic microcalorimeters.** More recently, magnetic microcalorimeters (MMCs) have emerged as an alternative to TES detectors. MMCs exploit the different occupancy of spin states in an Er-doped Au sensor at low temperature in an external magnetic field  $B \simeq k_B T / g \mu_B$ , and measure the change in magnetization upon X-ray absorption. Like TESs, MMCs are read out by SQUID preamplifiers, and multiplexing technology developed for TES readout can be adapted to read out future MMC arrays. Magnetic microcalorimeters provide higher energy resolution than resistive sensors, because there is no sensor heating from any bias current (Fig. 7). The thermal conductance to the cold bath and its associated noise can therefore in principle be made arbitrarily small, at the expense of a lower maximum count rate (Bühler *et al.*, 1994). The energy resolution is then limited to

$$\Delta E_{\text{FWHM}} \simeq 2.355 (4k_B T^2 C_{\text{abs}})^{1/2} (4\tau_0/\tau_1)^{1/4}, \quad (6)$$

where  $\tau_0 = C_{\text{abs}}/G_{\text{abs}} \simeq 0.1 \mu\text{s}$  is the time constant for coupling the photon energy from the phonons in the absorber to the spins in the thermistor, and  $\tau_1 = C_{\text{abs}}/G$  is the time constant for thermal coupling to the cold bath (Enss *et al.*, 2000; Fleischmann *et al.*, 2000). For well coupled absorber and spins  $\tau_1 \gg \tau_0$ , and magnetic calorimeters can thus have an energy resolution well below 1 eV for the same heat capacity as other cryogenic calorimeters, or significantly higher absorption efficiency at the same energy resolution. This currently comes at the price of a reduced count rate, since the thermal coupling between the cold bath and the sensor must be reduced to ensure  $\tau_1 \gg \tau_0$ . Current pulse decay times of order several milliseconds will likely be reduced in future designs, since they are too slow even for many high-energy astrophysics applications, one driver behind MMC development. It remains open if their speed can be improved to also enable novel synchrotron-based science (Enss *et al.*, 2004).

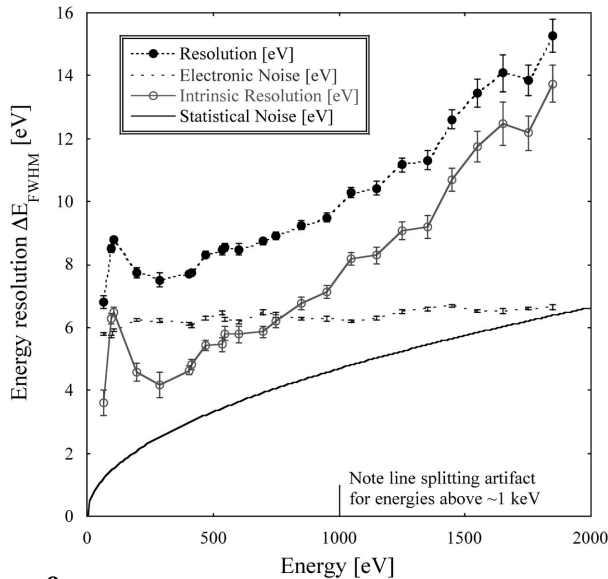
## 3.2. Athermal detectors: tunnel junctions

**3.2.1. Superconductor–insulator–superconductor tunnel junctions.** STJs consist of two superconducting electrodes separated by a thin insulating tunnel barrier. X-rays absorbed in one of the electrodes excite excess charge carriers above the superconducting energy gap  $\Delta$  in proportion to the X-ray energy  $E_x$ , which are measured as a temporary increase in tunneling current. Since the average energy to create an excess charge carrier  $\varepsilon \simeq 1.7\Delta$  scales with the energy gap  $\Delta$ , which is of the order of  $\sim 1 \text{ meV}$  and thus roughly a factor  $\sim 1000$  smaller than the gap in semiconductors, STJ detectors can have  $1000^{1/2} (\simeq 30)$  times better energy resolution than Si(Li) or Ge detectors (Kurakado, 1982). For increased absorption efficiency, a thick large-gap superconducting absorber is typically used in conjunction with a thin lower-gap tunnel junction that serves as a charge trap and confines the charges in a region close to the tunnel barrier. Also, charges are often kept from diffusing out of the counterelectrode by another large-gap superconductor, so that each carrier can tunnel multiple times, each time contributing charge in the same forward direction (Fig. 9, inset). On the one hand, this increases the total signal by the average number of tunneling events  $\langle n \rangle = \tau_{\text{rec}}/\tau_{\text{tun}}$ . On the other hand, it increases the pulse decay time by a factor  $\langle n \rangle$  and limits the fundamentally attainable energy resolution to

$$\Delta E_{\text{FWHM}} = 2.355 [\varepsilon E_x (F + 1 + 1/\langle n \rangle)]^{1/2}. \quad (7)$$

Here  $F \simeq 0.2$  is the Fano factor that describes the statistical fluctuations in the charge generation process, and  $1 + 1/\langle n \rangle$  quantifies the additional statistical noise due to variations in the number of average tunneling events each charge carrier undergoes (Mears *et al.*, 1993). Charge multiplication is therefore only advantageous if electronic noise sets the detector resolution, and if the detector sensitivity is not limited by its total count-rate capabilities. Still, even with charge multiplication by multiple tunneling, STJ detectors can theoretically have an energy resolution well below 10 eV FWHM for X-ray energies up to 10 keV. In practice, an energy resolution around 12 eV has been achieved at 6 keV (Angloher *et al.*, 2001; Li *et al.*, 2001), and an energy resolution between 2 and 9 eV for soft X-rays between 50 eV and 1 keV (Fig. 8) (le Grand *et al.*, 1998; Friedrich *et al.*, 1999; Kraft *et al.*, 1999; Verhoeve *et al.*, 2002). STJs have a comparably high dynamic resistance and capacitance, and can be read out with inexpensive FET-based low-noise preamplifiers operated at room temperature (Friedrich *et al.*, 1997).

STJs are the cryogenic detector technology that has been used most extensively in synchrotron-based research so far because of their comparably high count-rate capabilities of over  $10000 \text{ counts s}^{-1} \text{ pixel}^{-1}$  (Fig. 9) (Frank, Hiller *et al.*, 1998; Friedrich *et al.*, 2003). The maximum count rate is determined by the time that the excited excess charges remain in the junction area, either until they diffuse into the leads or until they recombine back into the superconducting ground state. In current devices, which increase the signal charge by a factor  $\langle n \rangle \simeq \tau_{\text{rec}}/\tau_{\text{tun}} \simeq 3$  by multiple tunneling, this time is set


**Figure 8**

STJ energy resolution as a function of X-ray energy in the soft X-ray band between 50 eV and 1 keV (solid circles). The electronic noise is due to increased IR-photon flux when operating the detector at the end of a cold finger behind three IR-blocking windows. The intrinsic noise (open circles), calculated by subtracting the electronic noise from the measured resolution in quadrature, approaches the statistical limit (solid line).

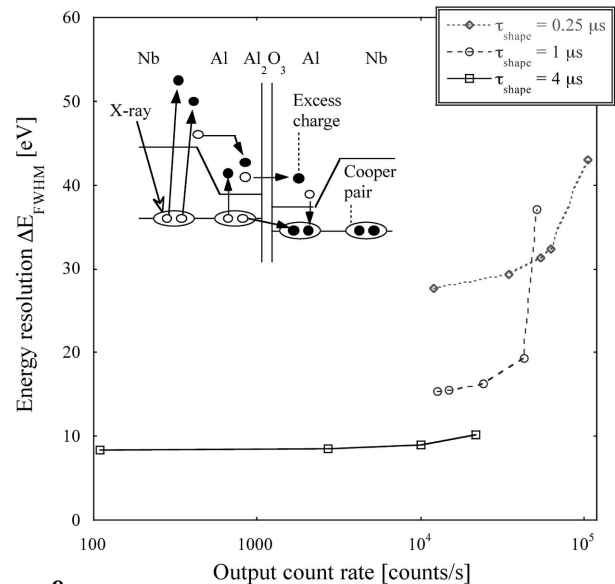
by the charge carrier recombination time of  $\tau_{\text{rec}} \simeq 3 \mu\text{s}$ . If desired, future devices can be designed for higher speed by using higher-transmissivity tunnel barriers with fast charge diffusion into the leads, in which case the tunneling time  $\tau_{\text{tun}}$  would set the maximum count rate.

### 3.2.2. Normal-insulator–superconductor tunnel junctions.

There was a brief period in the mid-1990s when tunnel junctions based on normal–insulator–superconductor (NIS) structures were developed as high-resolution X-ray detectors (Nahum & Martinis, 1995). Like STJs based on SIS junctions, NIS junction detectors are based on measuring the increase in tunneling current upon X-ray absorption. But since X-rays are absorbed in the normal conducting electrode where excitation energies  $\varepsilon$  are of the order of  $\sim k_{\text{B}}T \ll \Delta$ , the limiting energy resolution for NIS junction detectors,

$$\Delta E_{\text{FWHM}} \simeq 2.355(k_{\text{B}}T^2 C_{\text{abs}})^{1/2} \times \left\{ 1 + 0.4 \left[ \frac{G}{k_{\text{B}}(I_{\text{bias}}/e)} \right] \left( 1 + \frac{i_{n,\text{SQUID}}}{2eI_{\text{bias}}} \right) \right\}^{1/2}, \quad (8)$$

can be higher than for SIS junctions. Here,  $G$  is the total thermal conductance between the electrons in the absorber and the cold bath, ideally dominated by the thermal conductance  $G_{\text{el}} = k_{\text{B}}(I_{\text{bias}}/e)$  of the NIS junction itself. As low-impedance devices, NIS junctions also require a SQUID preamplifier readout, whose influence is negligible if its current noise  $i_{n,\text{SQUID}}$  is less than the shot noise of the detector bias current  $2eI_{\text{bias}}$ . Like thermal detectors, the speed of NIS junctions is set by a thermal decay time but, since the signal is carried by non-equilibrium electrons rather than phonons,  $\tau = C_{\text{abs}}/G_{\text{el}}$  can be as fast as  $10 \mu\text{s}$  (Nahum & Martinis, 1995). NIS junctions can therefore combine the high energy resolution of


**Figure 9**

Energy resolution as a function of count rate for an incident energy  $E_x = 277 \text{ eV}$ . Operation up to  $\sim 20000 \text{ counts s}^{-1} \text{ pixel}^{-1}$  is possible at the highest energy resolution, and operation up to  $\sim 100000 \text{ counts s}^{-1}$  is possible for shorter shaping times at reduced resolution. The inset shows the band diagram in Nb–Al–AlO<sub>x</sub>–Al–Nb STJ detectors and the charge flow upon X-ray absorption.

thermal detectors with the comparably high speed of tunneling devices. NIS junctions fell out of favor when TES microcalorimeters were invented, and few groups are currently advancing NIS junction development for X-ray detection. Still, they could be useful in synchrotron applications that require higher energy resolution than SIS junctions currently offer, and higher count rates than those of thermal detectors. Table 2 summarizes the performance of the main cryogenic detector technologies currently being developed.

## 4. Applications

### 4.1. Cryogenics

Cryogenic detector developers soon realised that their detectors would remain a niche technology available only to a few low-temperature experts unless detector operation at 0.1 K was made more user-friendly. Several groups have therefore developed refrigeration technology that is straightforward to operate and can be automated to attain 0.1 K base temperatures from 4.2 K at the push of a button. Most of the refrigerators are based on adiabatic demagnetization (ADRs), a process that involves the isothermal magnetization and adiabatic demagnetization of paramagnetic materials to cool below the He bath temperature of 4.2 K. Isothermal magnetization lowers the entropy of a paramagnet, and the attendant heat of magnetization is carried into the cold bath through a closed heat switch. After the system is equilibrated at 4.2 K, the heat switch is opened to thermally decouple the cold stage from the 4.2 K bath, and the magnetic field is decreased slowly keeping the entropy constant, thereby lowering the temperature. Typically, ADRs employ two different paramagnets to

**Table 2**

Comparison of energy resolution and count rate performance for different cryogenic detector technologies.

All values are order-of-magnitude estimates. Note the general trend of a trade-off between energy resolution and maximum total count rate.

Cryogenic detector Operating principle	Energy resolution		Count rate	
	Limiting $\Delta E_{\text{rms}}$	Target $\Delta E_{\text{FWHM}}$	Limiting rate	Target rate
Doped Si, NTD Ge $E_x \rightarrow \Delta T \rightarrow \Delta R$	$\xi (k_B T^2 C)^{1/2}$	$\Delta E \simeq \text{few eV}$	$\tau_0 \simeq C_{\text{abs}}/G$ $\tau \simeq 1 \text{ ms}$	$\sim 10 \text{ s}^{-1}$
TES transition edge sensors $E_x \rightarrow \Delta T \rightarrow \Delta R$	$[4k_B T^2 C(n/2)^{1/2}/\alpha]^{1/2}$	$\Delta E \simeq 1 \text{ eV}$	$\tau \simeq \tau_0/(\alpha/n)$ $\tau \simeq 100 \mu\text{s}$	$\sim 100 \text{ s}^{-1}$
Magnetic microcalorimeters $E_x \rightarrow \Delta T \rightarrow \Delta M$	$(4k_B T^2 C)^{1/2} (4G/G_{\text{abs}})^{1/4}$	$\Delta E \simeq 0.1 \text{ eV}$	$\tau \simeq C_{\text{abs}}/G_{\text{abs}}$ $\tau \simeq 1 \text{ ms}$	$\sim 10 \text{ s}^{-1}$
STJs $E_x \rightarrow \Delta Q \rightarrow \Delta I$	$[\varepsilon E_x (F + 1 + 1/(n))]^{1/2}$	$\Delta E \simeq 1\text{--}5 \text{ eV}$ at 0.5–6 keV	$\tau_{\text{rec}}$ or $\tau_{\text{tun}}$ $\tau_{\text{rec}} \simeq 1\text{--}100 \mu\text{s}$ $\tau_{\text{tun}} \simeq 0.1\text{--}1 \mu\text{s}$	$\sim 10000 \text{ s}^{-1}$
NIS tunnel junctions $E_x \rightarrow \Delta T \rightarrow \Delta I$	$1.4(k_B T^2 C)^{1/2}$	$\Delta E \simeq \text{few eV}$	$\tau \simeq C_{\text{abs}}/G_{\text{el}}$ $\tau \simeq 10 \mu\text{s}$	$\sim 1000 \text{ s}^{-1}$

avoid the need to pump on the He bath. One, typically a gallium gadolinium garnet (GGG), is used to cool a guard stage to  $\sim 1 \text{ K}$ , and a second one, usually iron ammonium sulfate, known as FAA for ferric ammonium alum, is used to cool the detector to  $\sim 0.1 \text{ K}$  (Fig. 10) (Hagmann & Richards, 1994; Friedrich *et al.*, 2001). ADRs are compact, reliable, easy to use and the demagnetization cycle can easily be automated.

The final step towards full automation is to replace the liquid  $\text{N}_2$  and He coolants used to pre-cool the spectrometer to 4.2 K by a mechanical cryocooler. Traditionally, mechanical coolers have produced significant vibrations, and microphonic interference has precluded operating them with high-resolution detectors. However, modern pulse-tube coolers have much lower vibrations since there are no mechanically moving parts in the cold head. Two-stage ADRs with pulse-tube pre-coolers are now commercially available, and have successfully been operated with high-resolution microcalorimeter X-ray detectors for defect analysis on semiconductor wafers (Simmnacher *et al.*, 2003). Only moderate modifications are necessary to adapt pulse-tube-based ADRs to the operation of tunnel junction detectors for synchrotron-based science, and tests towards this end are currently being conducted.

## 4.2. Detector characterization

Many of the initial experiments with cryogenic detectors were designed to characterize the detector response at different energies, count rates and absorption locations. Tunable monoenergetic synchrotron beams are ideal for determining the energy resolution as a function of energy. For Nb/Al-based STJs, values between 1.7 and 8.9 eV FWHM have been achieved for photon energies between 50 eV and 1 keV (Fig. 8) (le Grand *et al.*, 1998; Friedrich *et al.*, 1999), and in Ta-based devices an energy resolution between 1.2 eV and 11 eV for photon energies between 30 eV and 1.7 keV was measured (Kraft *et al.*, 1999). Al-based STJs with a 1.3  $\mu\text{m}$  Pb absorber, whose energy resolution of  $\sim 11 \text{ eV}$  at 6 keV makes them interesting for higher-energy operation, have also been characterized between 3 and 10 keV (Angloher *et al.*, 2001; Huber *et al.*, 2004).

Variable-exit-slit settings have been used to study detector resolution as a function of count rate. Signal rates above

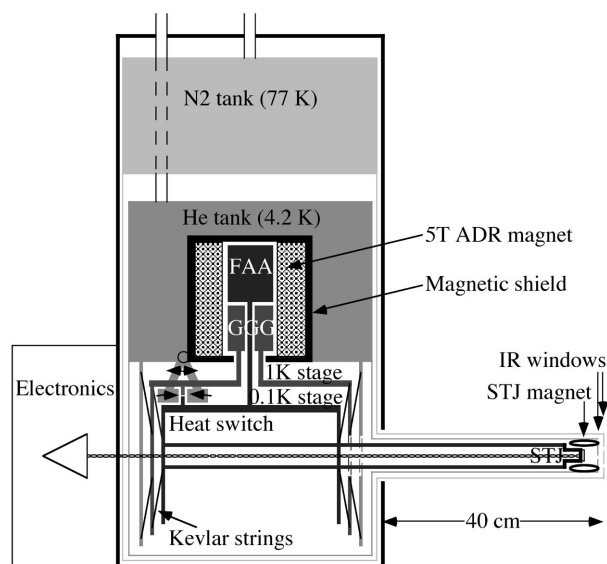


**Figure 10**

Schematic cross section of a two-stage ADR. The spectrometer is pre-cooled to 77 and 4.2 K using liquid  $\text{N}_2$  and He, which could be replaced by mechanical pulse-tube coolers in future spectrometer designs. The  $3 \times 3$  STJ detector array is held at the end of the cold finger at  $\sim 0.1 \text{ K}$  behind three IR-blocking windows within  $\sim 15 \text{ mm}$  of the room-temperature sample.

20000 counts  $\text{s}^{-1}$  are possible for STJ detectors at the highest energy resolution at a shaping time of 4  $\mu\text{s}$  (Fig. 9). Shorter shaping times allow operation up to  $\sim 100000$  counts  $\text{s}^{-1}$  per detector pixel at reduced resolution in Nb-based STJs, which tend to have shorter excess charge life-times ( $\tau_{\text{rec}}$ ) and therefore tend to be faster than Ta- or Pb/Al-based STJs (Frank, Hiller *et al.*, 1998; Friedrich *et al.*, 2001).

In addition, collimated X-ray beams have been used to measure spatial variations in the detector response. Fig. 11 illustrates these variations for a line scan across a  $140 \mu\text{m} \times 140 \mu\text{m}$  Nb-based STJ (Bechstein *et al.*, 2004). The response is reduced at either end due to increased charge loss at the device edges and due to charge diffusion into the leads. Such losses lead both to the broadening of lines and deviations from the ideal Gaussian detector response (Fig. 11, inset). They can be reduced by passivating the edges through anodization, or

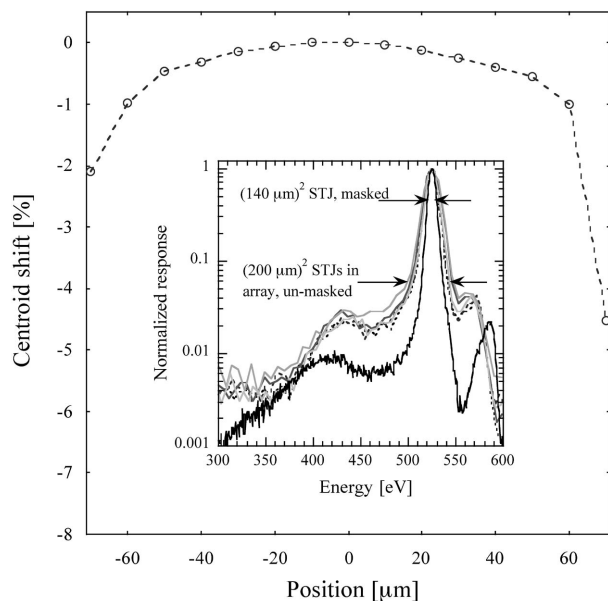


**Figure 11**

Spatial variations of the detector response in a  $140\ \mu\text{m} \times 140\ \mu\text{m}$  STJ detector (Bechstein *et al.*, 2004). The reduced peak height at the ends of the line scan is due to increased charge loss at the detector edges, and degrades the energy resolution and causes deviations from the Gaussian line shape (inset).

by collimating the incident X-rays through apertures. The fractional variation of the response is sufficiently small to be negligible at low energies, but it can become relevant for detector operation above several keV. Fig. 12, taken at a scanning SQUID microscope, visualizes the effects of trapped magnetic field quanta when an STJ detector is cooled through the superconducting transition in a small perpendicular magnetic field (Pressler *et al.*, 2000; Ohkubo *et al.*, 2002). Flux trapping creates normal-conducting regions with reduced response, visualized in Fig. 12 as dark dots, and increases the leakage current and thus the electronic noise. Similar detector characterization experiments have been performed on TES X-ray detectors, indicating at least equal sensitivity to external perpendicular magnetic fields and thus the need for good shielding during cool-down (Pressler *et al.*, 2002).

### 4.3. High-resolution X-ray spectroscopy

Cryogenic detectors have so far been used successfully for XRF and for fluorescence-detected XAS analysis. They have not yet been used for site- or spin-dependent XAS, nor for RIXS or R-ray Raman spectroscopy. This is not surprising since these experiments require higher energy resolution, and current high-resolution microcalorimeters do not yet have the required count-rate capabilities.

The Advanced Detector Group at Lawrence Livermore National Laboratory has developed cryogenic spectrometers with small  $3 \times 3$  STJ detector arrays for synchrotron science (Friedrich *et al.*, 2001). Two of their spectrometers are currently in use, one at the Advanced Biological and Environmental (ABEX) facility at the Advanced Light Source in Berkeley (USA), and one at the PTB Radiometry Laboratory

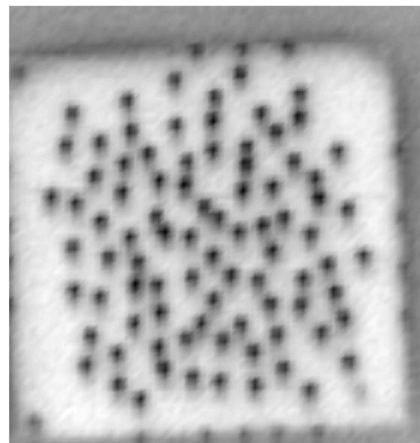


**Figure 12**

Scanning SQUID microscope picture of an STJ detector response at a perpendicular magnetic field of 23 mGauss (Ohkubo *et al.*, 2002). The dark dots indicate the presence of trapped flux quanta, which create charge trapping sites and cause a reduced detector response.

at the BESSY II synchrotron in Berlin (Germany) (Friedrich *et al.*, 2002; Veldkamp *et al.*, 2002; Bechstein *et al.*, 2004). They have been used for beamline characterization and for soft X-ray fluorescence analysis (Frank, Mears *et al.*, 1998; Veldkamp *et al.*, 2002). Synchrotron research with TES microcalorimeters is starting as well, although these TES spectrometers are not yet equipped with cold fingers to operate the TES close to the fluorescence sample (Maurizio *et al.*, 2004).

The first prominent scientific results with cryogenic (STJ) detectors employed them for fluorescence detection in X-ray absorption spectroscopy on dilute samples to measure oxidation states and electronic structure. Understanding the chemistry of dilute specimens is important in diverse applications ranging from material science to biochemistry, and the increased sensitivity that cryogenic detectors offer makes them widely useful, both for spectroscopy on light-element *K*-edges (Fig. 4) and for transition metal *L*-edges (Fig. 6). In material science, for example, XAS can be used to understand the chemistry of dopants in novel semiconductors or nanomaterials and their changes upon sample processing. STJ spectrometers have been used to examine the role of nitrogen in GaInNAs III–V semiconductors, and to attribute an observed band-gap increase upon annealing to increased In–N bonding (Lordi *et al.*, 2003). In biochemistry, metals serve as catalysts in many proteins, and STJ spectrometers have been employed to examine the oxidation state of Ni in the active site of CO-binding ACDS protein (Funk *et al.*, 2004). In environmental science, oxidation states determine metal solubility and thus their bioavailability and toxicity, and first experiments on chromium speciation in environmental contaminations from welding operations have been performed at the ABEX facility at the ALS (Friedrich *et al.*, 2006). The importance that these metals play at the interface between biochemistry and environmental science and their relevance in geochemistry is driving a current push towards applications in the geological sciences. These experiments have changed the

perception of cryogenic detectors from laboratory curiosities to powerful instruments for SR-XRF. Other experiments are certain to follow, with the possibility of providing a driving force for cryogenic detector research independent of particle astrophysics that has traditionally dominated this field.

## 5. Summary and outlook

Cryogenic X-ray detectors are a class of energy-dispersive spectrometers operated at temperatures of  $\sim 0.1$  K that provide more than an order of magnitude improvement in energy resolution compared with conventional Ge or Si(Li) detectors. This comes at a price of reduced pixel area, typically of order  $200 \mu\text{m} \times 200 \mu\text{m}$ , and count-rate capabilities, which vary between tens and ten thousands of counts  $\text{s}^{-1}$  for the different cryogenic detector technologies. In general, there is a trade-off between highest energy resolution and high count-rate capabilities. Microcalorimeter detectors provide the highest energy resolution, currently around 2.5 eV FWHM at 6 keV with a possible future performance below 1 eV, but can only be operated at tens to hundreds of counts  $\text{s}^{-1}$ . STJ detectors provide somewhat lower energy resolution, currently around 12 eV FWHM at 6 keV and 5–10 eV at 0.5 keV, but can be operated at count rates above 20000 counts  $\text{s}^{-1} \text{pixel}^{-1}$ . Two-stage adiabatic demagnetization refrigerators make detector operation at  $\sim 0.1$  K comparably user-friendly, and future adaptations of mechanical pulse-tube cryocoolers for push-button operation will make the detector technology widely available also to non-experts.

In synchrotron science, where the tunable monochromatic incident beam can provide natural-linewidth limited spectra, STJ detectors have so far found more applications. Most prominently, they are being used for fluorescence-detected X-ray absorption spectroscopy at light-element *K*-edges and transition metal *L*- and *M*-edges. These measurements are designed to determine chemical states of dilute elements, and cryogenic STJ detectors can greatly increase the sensitivity for these measurements in the soft X-ray region. This has so far been used in biophysics and material science applications, with additional applications in environmental science and geology currently being pursued. We note that high-efficiency cryogenic detectors can make older low-flux beamlines competitive again for the analysis of samples that would suffer from radiation damage during  $\sim 1$  h XAS scans at modern undulator beamlines.

Cryogenic detector development is focusing on improving their sensitivity, mostly by research in four areas:

(i) The STJ array size is currently being increased from  $3 \times 3$  to  $6 \times 6$  pixels, with  $10 \times 10$  arrays being planned and  $100 \times 100$  arrays possible. While 100-pixel arrays can still be operated in adiabatic demagnetization refrigerators, the heat load into the cold stage due to the wiring connections in much larger arrays will require the cooling power of dilution refrigerators.

(ii) High-*Z* absorbers like Ta and Pb are likely to be incorporated in future STJ designs to increase the detector's

quantum efficiency and extend their range of operation to hard X-rays.

(iii) Polycapillary point-to-point X-ray focusing optics between the sample and the detector array can further enhance the solid-angle coverage of cryogenic detectors. Optics also allow coupling cryogenic detectors to samples over some distance in cases where it is not possible to place the detector in close proximity. Examples include X-ray microscopes, diamond anvil cells for high-pressure studies, or high magnetic field regions for X-ray magnetic circular dichroism measurements.

(iv) While microcalorimeter research is currently driven by the needs of X-ray astrophysics, the expected advances in energy resolution and count-rate capabilities could make this technology also interesting for synchrotron science. The current target for the planned Constellation-X astronomy mission includes a  $\sim 1000$ -pixel microcalorimeter array with  $\sim 2$  eV FWHM resolution at 6 keV that can be operated at  $\sim 1000$  counts  $\text{s}^{-1} \text{pixel}^{-1}$ . Such an instrument would probably enable site- or spin-dependent XAS on certain samples, and extend RIXS studies to more dilute samples than currently possible.

Over the last decades, synchrotron science has been driven by the desire to build brighter sources. This drive was immensely successful, to the point that many interesting samples are now damaged in experiments with bright modern synchrotron beams. Improving the detector technology is an alternative path to extract novel science from existing sources, and cryogenic detectors are likely to play a major role on this path.

We thank Simon J. George and Ben and Nick's Porter for stimulating discussions on scientific uses of cryogenic detectors. We also thank Sylke Bechstein, Burkhard Beckhoff, Jonathan Denlinger, Christian Enss, Masataka Ohkubo and Scott Porter for providing original data. This work was performed under the auspices of the US Department of Energy by University of California Lawrence Livermore National Laboratory under contract No. W-7405-Eng-48.

## References

- d'Acapito, F. & Maurizio, C. (2004). *Nucl. Instrum. Methods*, **520**, 602–605.
- Andrews, D. H., Brucksch, W. F. Jr, Ziegler, W. T. & Blanchard, E. R. (1942). *Rev. Sci. Instrum.* **13**, 281–292.
- Angloher, G., Hettl, P., Huber, M., Jochum, J., v. Feilitzsch, F. & Mößbauer, R. L. (2001). *J. Appl. Phys.* **89**, 1425–1427.
- Bandler, S., Silver, E., Schnopper, H., Murray, S., Barbera, M., Madden, N., Landis, D., Beeman, J., Haller, E. & Tucker, G. (2000). *Nucl. Instrum. Methods*, **444**, 273–277.
- Bechstein, S., Beckhoff, B., Fliegau, R., Weser, J. & Ulm, G. (2004). *Spectrochim. Acta B*, **59**, 215–221.
- Bergmann, U. & Cramer, S. P. (1999). *Proc. SPIE*, **3448**, 198–209.
- Bergmann, U., Glatzel, P., Robblee, J. H., Messinger, J., Fernandez, C., Cinco, R., Visser, H., McFarlane, K., Bellacchio, E., Pizarro, S., Sauer, K., Yachandra, V. K., Klein, M. P., Cox, B. L., Neelson, K. H. & Cramer, S. P. (2001). *J. Synchrotron Rad.* **8**, 199–203.
- Bergmann, U., Horne, C. R., Collins, T. J., Workman, J. M. & Cramer, S. P. (1999). *Chem. Phys. Lett.* **302**, 119–124.

- Bühler, M., Umlauf, E. & Mather, J. C. (1994). *Nucl. Instrum. Methods A*, **346**, 225–229.
- Cramer, S. P., DeGroot, F. M. F., Ma, Y., Chen, C. T., Sette, F., Kipke, C. A., Eichhorn, D. M., Chan, M. K. & Armstrong, W. H. (1991). *J. Am. Chem. Soc.* **113**, 7937–7940.
- Cunningham, M. F., Ullom, J. N., Miyazaki, T., Labov, S. E., Clarke, J., Lanting, T. M., Lee, A. T., Richards, P. L., Yoon, J. & Spieler, H. (2002). *Appl. Phys. Lett.* **81**, 159–161.
- Drury, O. B. & Friedrich, S. (2005). *IEEE Trans. Appl. Superconduct.* **15**, 613–617.
- Enss, C., Fleischmann, A., Bandler, S. R., Stevenson, T. R. & Seidel, G. M. (2004). *Nucl. Instrum. Methods A*, **520**, 407–410.
- Enss, C., Fleischmann, A., Horst, K., Schönefeld, J., Sollner, J., Huang, Y. H., Kim, Y. H., Adams, J. S. & Seidel, G. M. (2000). *J. Low Temp. Phys.* **121**, 137–177.
- Fleischmann, A., Daniyarov, T., Rotzinger, H., Linck, M., Enss, C. & Seidel, G. M. (2003). *Rev. Sci. Instrum.* **74**, 3947–3954.
- Fleischmann, A., Link, M., Daniyarov, T., Rotzinger, H., Enss, C. & Seidel, G. M. (2004). *Nucl. Instrum. Methods A*, **520**, 27–31.
- Frank, M., Friedrich, S., Höhne, J. & Jochum, J. (2003). *J. X-ray Sci. Technol.* **11**, 83–112.
- Frank, M., Hiller, L. J., le Grand, J. B., Mears, C. A., Labov, S. E., Lindeman, M. A., Netel, H., Chow, D. & Barfknecht, A. T. (1998). *Rev. Sci. Instrum.* **69**, 25–31.
- Frank, M., Mears, C. A., Labov, S. E., Hiller, L. J., le Grand, J. B., Lindeman, M. A., Netel, H., Chow, D. T. & Barfknecht, A. T. (1998). *J. Synchrotron Rad.* **5**, 515–517.
- Friedrich, S., Drury, O. B., Cramer, S. P. & Green, P. G. (2006). *Nucl. Instrum. Methods A*. Accepted.
- Friedrich, S., Funk, T., Drury, O., Labov, S. E. & Cramer, S. P. (2002). *Rev. Sci. Instrum.* **73**, 1629–1631.
- Friedrich, S., le Grand, J. B., Hiller, L. J., Kipp, J., Frank, M., Labov, S. E., Cramer, S. P. & Barfknecht, A. T. (1999). *IEEE Trans. Appl. Superconduct.* **9**, 3330–3333.
- Friedrich, S., Niedermayr, T., Drury, O., Cunningham, M. F., van den Berg, M. L., Ullom, J. N., Funk, T., Cramer, S. P., Batteux, J. D., See, E., Frank, M. & Labov, S. E. (2001). *Nucl. Instrum. Methods*, **467**, 1117–1120.
- Friedrich, S., Segall, K., Gaidis, M. C., Wilson, C. M., Prober, D. E., Kindlmann, P. J., Szymkowiak, A. E. & Moseley, S. H. (1997). *IEEE Trans. Appl. Superconduct.* **7**, 3383–3386.
- Friedrich, S., Vailionis, A., Drury, O., Niedermayr, T., Funk, T., Kang, W. N., Choi, E. M., Kim, H. J., Lee, S. I., Cramer, S. P., Kim, C. & Labov, S. E. (2003). *IEEE Trans. Appl. Superconduct.* **13**, 1114–1119.
- Funk, T., Gu, W., Friedrich, S., Wang, H., Gencic, S., Grahame, D. A. & Cramer, S. P. (2004). *J. Am. Chem. Soc.* **126**, 88–95.
- Gatti, F. (2004). Editor. *Proceedings of the 10th International Workshop on Low Temperature Detectors, LTD-10*. (*Nucl. Instrum. Methods A*, **520**, 1–685.)
- Grand, J. B. le, Mears, C. A., Hiller, L. J., Frank, M., Labov, S. E., Netel, H., Chow, D., Friedrich, S., Lindeman, M. A. & Barfknecht, A. T. (1998). *Appl. Phys. Lett.* **73**, 1295–1297.
- Groot, F. M. F. de, Fuggle, J. C., Thole, B. T. & Sawatzky, G. A. (1990). *Phys. Rev. B*, **42**, 5459–5468.
- Grush, M. M., Christou, G., Haemaelaenen, K. & Cramer, S. P. (1995). *J. Am. Chem. Soc.* **117**, 5895–5896.
- Hagmann, C. & Richards, P. L. (1994). *Cryogenics*, **34**, 221–226.
- Hoovers, H. F. C., Bento, A. C., Bruijn, M. P., Gottardi, L., Korevaar, M. A. N., Mels, W. A. & de Korte, P. A. J. (2000). *Appl. Phys. Lett.* **77**, 4422–4424.
- Huber, M., Bechstein, S., Beckhoff, B., v. Feilitzsch, F., Jochum, J., Krumrey, M., Rudig, A. & Ulm, G. (2004). *Nucl. Instrum. Methods A*, **520**, 234–236.
- Irwin, K. D. (1995). *Appl. Phys. Lett.* **66**, 1998–2000.
- Irwin, K. D. (2002). *Physica C*, **368**, 203–210.
- Irwin, K. D., Hilton G. C., Wollman, D. A. & Martinis, J. M. (1998). *J. Appl. Phys.* **83**, 3978–3985.
- Jaklevic, J., Kirby, J. A., Klein, M. P., Robertson, A. S., Brown, G. S. & Eisenberger, P. (1977). *Solid State Commun.* **23**, 679–682.
- Kotani, A. & Shin, S. (2001). *Rev. Mod. Phys.* **73**, 203–246.
- Kraft, S., Verhoeve, P., Peacock, A., Rando, N., Goldie, D. J., Hart, R., Glowacka, D., Scholze, F. & Ulm, G. (1999). *J. Appl. Phys.* **86**, 7189–7191.
- Krause, M. O. (1979). *J. Phys. Chem. Ref. Data*, **8**, 307–327.
- Kurakado, M. (1982). *Nucl. Instrum. Methods*, **196**, 275–277.
- Lepy, M. C., Campbell, J. L., Laborie, J. M., Plagnard, J., Stemmler, P. & Teesdale, W. J. (2000). *Nucl. Instrum. Methods A*, **439**, 239–246.
- Li, L., Frunzio, L., Wilson, C., Prober, D. E., Szymkowiak, A. E. & Moseley, S. H. (2001). *J. Appl. Phys.* **90**, 3645–3646.
- Lordi, V., Gambin, V., Friedrich, S., Funk, T., Takizawa, T., Uno, K. & Harris, J. S. (2003). *Phys. Rev. Lett.* **90**, 145505–145508.
- Maurizio, C., Pergolesi, D., Gatti, F., d’Acapito, F., Razeti, M., Balerna, A. & Mobilio, S. (2004). *Nucl. Instrum. Methods A*, **520**, 610–612.
- Mears, C. A., Labov, S. E. & Barfknecht, A. T. (1993). *Appl. Phys. Lett.* **63**, 2961–2963.
- Moseley, S. H., Mather, J. C. & McCammon, D. (1984). *J. Appl. Phys.* **56**, 1257–1262.
- Nahum, M. & Martinis, J. M. (1995). *Appl. Phys. Lett.* **66**, 3203–3205.
- Nordgren, J. & Guo, J. (2000). *J. Electron Spectrosc. Relat. Phenom.* **110–111**, 1–13.
- Ohkubo, M., Suzuki, K., Tanabe, K., Pressler, H. & Ukibe, M. (2002). *AIP Conf. Proc.* **605**, 55–58.
- Peng, G., de Groot, F. M. F., Haemaelaenen, K., Moore, J. A., Wang, X., Grush, M. M., Hastings, J. B., Siddons, D. P., Armstrong, W. H. et al. (1994). *J. Am. Chem. Soc.* **116**, 2914–2920.
- Porter, F. S., Brown, G. V. & Cottam, J. (2005). *Low Temperature Detectors*, edited by C. Enss. Berlin: Springer.
- Pressler, H., Koike, M., Ohkubo, M., Fukuda, D., Noguchi, Y., Ohno, M., Takahashi, H. & Nakazawa, M. (2002). *Appl. Phys. Lett.* **81**, 331–333.
- Pressler, H., Ohkubo, M., Koike, M., Ukibe, M., Zama, T., Nakamura, T. & Katagiri, M. (2000). *Appl. Phys. Lett.* **77**, 4055–4057.
- Ryder, P. L. (1977). *Scanning Electron Microsc.* **1**, 273–280.
- Silver, E. et al., (2000). *Astrophys. J.* **541**, 495–500.
- Simmacher, B., Weiland, R., Höhne, J., v. Feilitzsch, F. & Hollerith, C. (2003). *Microelectron. Reliab.* **43**, 1675–1680.
- Stahle, C. K., Allen, C. A., Boyce, K. R., Brekosky, R. P., Brown, G. V., Cottam, J., Figueroa-Feliciano, E., Galeazzi, M., Gygax, J. D., Jacobson, M. B., Kelley, R. L., Liu, D., McCammon, D., McClanahan, R. A., Moseley, S. H. et al. (2004). *Nucl. Instrum. Methods A*, **520**, 466–468.
- Stahle, C. K., Osheroff, D., Kelley, R. L., Moseley, S. H. & Szymkowiak, A. E. (1992). *Nucl. Instrum. Methods A*, **319**, 393–399.
- Ullom, J. N., Beall, J. A., Doriese, W. B., Duncan, W. D., Ferreira, L., Hilton, G. C., Irwin, K. D., Reintsema, C. D. & Vale, L. R. (2005). *Appl. Phys. Lett.* **87**, 194103–194105.
- Veldkamp, M., Beckhoff, B., Fliegau, R., Ulm, G., Frank, M., Friedrich, S. & Labov, S. E. (2002). *Nucl. Instrum. Methods A*, **487**, 450–456.
- Verhoeve, P., Rando, N., Peacock, A., Martin, D. & den Hartog, R. (2002). *Opt. Eng.* **41**, 1170–1184.
- Wollman, D. A., Nam, S. W., Hilton, G. C., Irwin, K. D., Bergren, N. F., Rudman, D. A., Martinis, J. M. & Newbury, D. E. (2000). *J. Microsc.* **199**, 37–44.